## IDETC2023-115068

# ROBUST TOPOLOGY OPTIMIZATION OF SYNCHRONOUS RELUCTANCE MOTORS USING CARDINAL BASIS FUNCTION BASED LEVEL SET METHOD

Jiawei Tian<sup>1</sup>, David Torrey<sup>2</sup>, Fang Luo<sup>3</sup>, Jon Longtin<sup>1</sup>, Shikui Chen<sup>1,\*</sup>

Department of Mechanical Engineering<sup>1</sup>

Department of Electrical and Computer Engineering<sup>3</sup>

State University of New York at Stony Brook, Stony Brook, New York, USA, 11794

GE Research<sup>2</sup>, Niskayuna, New York, USA, 12309

Email: {Jiawei.Tian, Fang.Luo, Jon.Longtin, Shikui.Chen}@stonybrook.edu; torrey@ge.com

#### **ABSTRACT**

Synchronous reluctance motors (SynRMs) have gained considerable attention in the field of electric vehicles as they reduce the need for permanent magnets in the rotor, resulting in less material and manufacturing costs. However, their lower average torque and torque ripple vibrations have been identified as key issues that require resolution. In this study, we present a SynRM design framework employing the cardinal basis functions (CBF)based parametric level set method. The SynRms design problem is recast as a variational problem constrained by Maxwell's equations which describe the behavior of electric and magnetic fields in the SynRM. A continuum shape sensitivity analysis is carried out using the material derivative and adjoint method. A distance regularization energy function is employed to maintain the level set function as a signed distance function during the optimization. The parametric topology optimization problem is computationally solved using the Method of Moving Asymptotes (MMA). To demonstrate the effectiveness of our approach, we present a numerical example that compares the torque characteristics of the optimal design with those of a reference design. Preliminary results show that the optimized SynRM has a 30.30% increase in average torque, along with a slight increase in torque ripple, compared to the reference model.

#### 1 Introduction

The recent focus in motor design has shifted towards increasing efficiency, reducing cost, and improving environmental friendliness [1]. Having no permanent magnets in the rotor, synchronous reluctance motors (SynRMs) can offer lower material and manufacturing costs [2]. In view of this, synchronous reluctance motors are an attractive option for industrial applications such as pumps, fans, traction, and electric vehicles.

In contrast to the permanent magnet (PM) machines [3], synchronous reluctance motors generate torque utilizing magnetic reluctance variation [4]. While SynRMs avoids the usage of PM in its structures, their limitations can not be ignored. One major disadvantage of SynRMs is their relatively lower average torque compared to other types of motors, including induction motor (IM) [5], permanent magnet synchronous motor (PMSM) [6]. Additionally, SynRMs suffer from torque ripple due to the interaction between the spatial harmonics of magnetomotive force (MMF) and the rotor geometry [7]. Theoretically, the torque performance of SynRM depends on the excitation current and the motor design itself [8]. Consequently, there is a need to identify the optimal layout of the rotor to improve the torque characteristics. Traditionally, design optimization of electric machines is based on the parameterized studies [9], which focus on finding the optimized shape and size, providing limited flexibility.

Because gradient-based topology optimization (TO) pro-

<sup>\*</sup>Address all correspondence to this author.

vides higher flexibility, several studies have been conducted on topology optimization for SynRMs. Notably, Lee et al. [10, 11] implemented a density-based topology optimization framework to determine an optimized layout for the iron webs and bridges of SynRMs. This work considers multiple aspects, including torque performance, manufacturability, and structural safety, as simultaneous optimization objectives. Additionally, Lee et al. [8] efficiently incorporated a design-dependent current phase angle into the topology optimization process for SynRMs. Okamoto et al. [12] employed an MMA-based TO method to optimize the rotor core layout of SynRMs, with a focus on enhancing the torque performance of and investigating the impact of the rotor bridges. Yamashita et al. [13] applied the level set method to designing SynRMs for reduced iron loss and improved torque characteristics. Park et al. [14,15] employed the level set method to improve the average torque by maximizing the magnetic energy between two rotor positions. In [16], the rotor of SynRMs was optimized using the ON/OFF method, and the iron loss, including eddy current loss and hysteresis loss, were newly considered in the optimization. Besides SynRMs, topology optimization for permanent magnet machines has been implemented using a number of methods, including bidirectional evolutionary structural optimization (BESO) [17, 18], level set method [19, 20] and densitybased methods [21, 22].

Topology optimization for electric machine design is currently in an active research area, and it entails a number of challenges that need to be addressed. The optimized result using the density-based method usually accompanies by the intermediate value and blurring boundaries, and the On-Off approach usually generates the checkerboard pattern [23]. These drawbacks will bring about troubles for further manufacturing. Although the filter projection can partly mitigate this issue and improve the optimized design's manufacturability, the selection of appropriate filtering radius directly affects the patterns of the optimization results [24]. A common way is conducting the parametric study to investigate the effects of various filtering radii on the optimized result, which is time-consuming [8]. Since the level set method directly evolves the design boundary [25], it can ensure a clear boundary in the final design and lessen the need for postprocessing. However, for the conventional level set approach, to guarantee the boundary evolves one grid interval length per time step, the step size needs to be sufficiently small. This will cause an excessive number of iterations before the objective function converges. Additionally, the conventional level set method requires the design velocity field extension to the whole design domain, which results in additional computational costs.

In view of this, we propose a cardinal basis function (CBF) based level set method to design SynRMs. By parameterization of level set function with cardinal basis function (CBF), we can transform the original Hamilton-Jacobi PDE into a system of ODE to lessen the computational burden [26, 27]. In addition, the reinitialization scheme in the conventional level set method

is replaced by the minimization of a distance regularization energy function along with the objective function [28]. This avoids the undesirable periodical suspension in the optimization process. With the parameterization of the level set function, the advanced optimization solver, such as Method of Moving Asymptotes (MMA) [29], can be employed to find the optimal design. The convergence speed can remarkably improve with these pros brought by the CBF-based level set method.

The rest of the paper is organized as follows: Section.2 introduces the modeling of synchronous reluctance motors (SynRMs). Section.3 presents the details on topology optimization of SynRMs, including cardinal basis function (CBF) based level set method, problem formulation, and shape sensitivity analysis, followed by one numerical example given in Section.4. Section.5 concludes the paper and outlines perspective work.

## 2 Modeling of Synchronous Reluctance Motors (Syn-RMs)

The SynRM consists of a laminated steel rotor and a laminated stator excited by a poly-phase winding. The winding is typically an integral slot winding, though a fractional slot winding could be applied. This study uses a four-pole SynRM as the numerical design model for topology optimization. The 2D geometry of the quarter SynRM model is illustrated in Fig.1, which is driven by balanced three-phase currents  $i_u(t)$ ,  $i_v(t)$  and  $i_w(t)$ :

$$i_{u}(t) = I_{m} \sin(\omega_{c}t - \theta)$$

$$i_{v}(t) = I_{m} \sin\left(\omega_{c}t - \frac{2\pi}{3} - \theta\right)$$

$$i_{w}(t) = I_{m} \sin\left(\omega_{c}t + \frac{2\pi}{3} - \theta\right) ,$$

$$(1)$$

where  $I_m$  is the amplitude of the current set to 120 A. The current phase angle  $\theta$  is set as  $\pi/3$  during the optimization process. The rotor rotates with a rotational velocity 1200r/min. The active length of this SynRM is 80mm. The radial airgap length is 5 mm. For the material properties, a linear material with relative permeability  $\mu_r$  is set 5000 for the rotor iron, where the design domain is placed. Although local magnetic saturation brought by the nonlinear constitutive relation between magnetic flux density **B** and magnetic field strength **H** will impact the magnetic performance, a linear relation is adopted at the current stage. This is because incorporating the nonlinearity into the current optimization model will overly complicate the shape sensitivity analysis, especially for solving the adjoint equation. To evaluate the effect of relative permeability, it is advisable to consider different relative permeability values. For the non-design area, the nonlinear soft iron is chosen for the stator. A copper electrical conductivity of  $6 \times 10^7$  S/m is used for the coils.

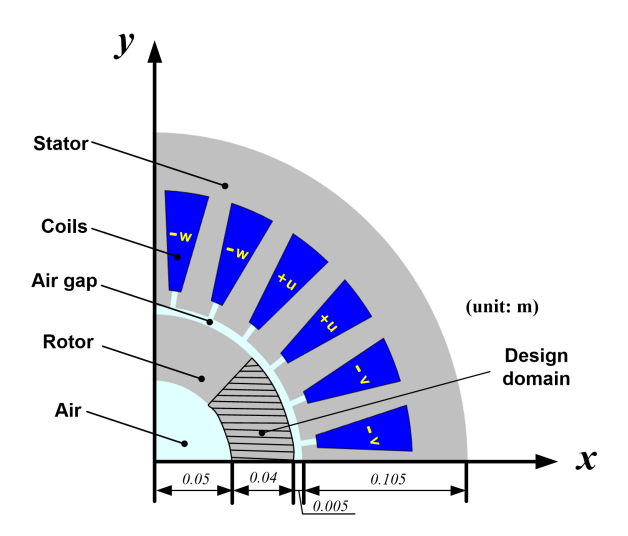


**FIGURE 1**: CAD model of synchronous reluctance motors (Syn-RMs).

Rotor rotation is modeled using the embedded physics interface for rotating machinery in COMSOL Multiphysics, where the sliding mesh interface facilitates the separation of the rotor and the stator. In addition, an anti-periodic boundary condition is applied to both sides of the geometry, as depicted in Fig. 1.

## 3 Topology Optimization of Synchronous Reluctance Motors (SynRMs)

#### 3.1 Conventional Level Set Method

Conventionally, the level set function  $\Phi$  is a Lipschitz continuous real-valued function defined in  $\mathbb{R}^2$  or  $\mathbb{R}^3$  [30]. With the level set method, the structure boundary  $\partial\Omega$ , highlighted as the red curve, is implicitly represented by the zero isosurface of the level set function with one-higher dimension, as illustrated in Fig. 2. According to the sign of the level set function, the design domain D can be divided into three parts, indicating the material, the interface, and the void, respectively. The level-set representation can be formulated as Eq. 2:

$$\begin{cases} \Phi(x,t) > 0, & x \in \Omega, & \text{material} \\ \Phi(x,t) = 0, & x \in \partial\Omega, & \text{boundary} \\ \Phi(x,t) < 0, & x \in D/\Omega, & \text{void} \end{cases}$$
 (2)

where x is the coordinates of an arbitrary point in the design domain and t is a pseudo time for the dynamic shape optimization process. The motion of the material interface is governed by the Hamilton-Jacobi equation:

$$\frac{\partial \Phi(x,t)}{\partial t} - V_n |\nabla \Phi(x,t)| = 0, \tag{3}$$

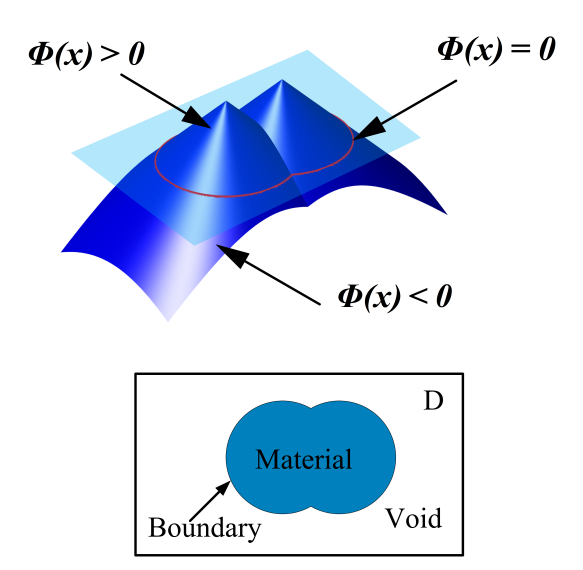


**FIGURE 2**: A schematic of level set representation.

where  $V_n$  is the normal velocity field contributing to the shape variation.

#### 3.2 CBF-Based Parametric Level Set Method

In this section, a cardinal basis function (CBF) is constructed based on the radial basis function partition of unity (RBF-POU) collocation method to parameterize the level set function [31]. For the derivations of CBF construction using RBF, see [27] and the references cited therein. Given n different nodes  $x_1, x_2, ..., x_n \in \mathbb{R}^2$  or  $\mathbb{R}^3$ , a level set function can be generally interpolated with cardinal basis functions (CBFs) in the following form,

$$\Phi(x,t) = \sum_{j=1}^{n} \Psi_j(\mathbf{x}) \mu_j(t), \tag{4}$$

where  $\mu_j(t)$  is actually the value of level set function at  $j_{th}$  node.  $\Psi_j(x)$  is the constructed CBF, which is equal to 1 at the center node and 0 at other nodes. The CBF with this Kronecker delta properties can be expressed as follows:

$$\Psi_j(x_i) = \begin{cases} 1, & i = j \\ 0, & i \neq j \end{cases}$$
 (5)

After the parameterization of the level set function using CBF, the design variable at each node owns obvious physical meaning, which is, namely, the value of the level set function. By substituting the Eq. 4 into the Hamilton-Jacobi Eq. 3, the original PDE is converted to an ODE in the following form,

$$\sum_{j=1}^{n} \dot{\mu}_j(t) \Psi_j(\mathbf{x}) - V_n |\nabla \Phi| = 0.$$
 (6)

From the above equation, the normal velocity field  $V_n$  can be obtained as follows:

$$V_n = \frac{1}{|\nabla \Phi|} \sum_{j=1}^n \dot{\mu}_j(t) \Psi_j(\mathbf{x}). \tag{7}$$

#### 3.3 Problem Formulation

The design target is to improve the average torque of SynRM and reduce its torque ripple simultaneously. In this study, the torque ripple can be measured as variance *Var*, and the average torque and the torque ripple can be expressed as follows:

$$E(T_i) = \frac{1}{n} \sum_{j=1}^{n} T_i \quad , \tag{8}$$

$$Var(T_i) = \frac{1}{n} \sum_{i=1}^{n} (T_i - E(T_i))^2$$
 , (9)

where  $T_i$  is the torque at the  $i_{th}$  rotor position. Thus, the optimization objective can be formulated to maximize the mean of the torque and minimize its variance, which can be expressed as:

Maximize: 
$$F = E(T_i) - Var(T_i)$$
,  
Subject to:  $a(A, \overline{A}) = l(\overline{A})$ ,  $\forall \overline{A} \in U$  (10)  
 $V(\Omega) = V^*$ ,

where  $V(\Omega)$  is the volume ratio of iron and  $V^*$  is the target volume ratio. The energy bilinear form  $a(A, \overline{A})$ , the source linear form  $l(\overline{A})$  of magnetostatic system without permanent magnet and the volume of iron  $V(\Omega)$  are described by:

$$a(\mathbf{A}, \overline{\mathbf{A}}) = \int_{\Omega} v \mathbf{B}(\mathbf{A}) \cdot \mathbf{B}(\overline{\mathbf{A}}) d\Omega$$
 , (11a)

$$l(\overline{A}) = \int_{\Omega} \boldsymbol{J} \cdot \overline{A} d\Omega \quad , \tag{11b}$$

$$V(\Omega) = \int_{\Omega} H(\Phi) d\Omega$$
 , (11c)

where  $H(\Phi)$  represents the Heaviside function and v,  $\mathbf{B}$  and  $\mathbf{J}$  represent the magnetic reluctivity, magnetic flux density, and current density, respectively.  $\mathbf{A}$  is the magnetic vector potential, and the arbitrary virtual vector potential  $\overline{\mathbf{A}}$  belongs to the space of admissible vector potential U:

$$U = \{ \overline{\mathbf{A}} \in [H^1(\Omega)] \mid \overline{\mathbf{A}} = 0 \text{ on } \mathbf{x} \in \Gamma \} \quad , \tag{12}$$

where  $\Gamma$  denotes the Dirichlet essential boundary and  $H^1(\Omega)$  represents the Sobolev space of first-order [32].

For accurate interpolation of material properties and effective avoidance of numerical instability during the optimization process [26, 27], a distance regularization energy function is introduced here. This function needs to be minimized along the objective function to maintain the distance-regularized level set function. The distance regularization energy function R is given in the following form:

$$R = \int_{\Omega} P(|\nabla \Phi|) d\Omega \quad , \tag{13}$$

where  $P(|\nabla \Phi|)$  is the regularization energy potential density, which is proposed by Li et al. [28] and formulated as follows:

$$P = \begin{cases} \frac{1}{(2\pi)^2} \left( 1 - \cos(2\pi |\nabla \Phi|) \right), & |\nabla \Phi| < 1 \\ \frac{1}{2} \left( |\nabla \Phi| - 1 \right)^2, & |\nabla \Phi| > 1 \end{cases}$$
 (14)

## 3.4 Shape Sensitivity Analysis

This section details how to conduct the shape sensitivity using the material time derivative. For the derivation, a general magneto-static system is considered, and the whole magneto-static system can be divided into two sub-domains  $\Omega_1$  and  $\Omega_2$  with the interface of  $\gamma$ , shown in Fig. 3. The domain  $\Omega_1$  and  $\Omega_2$  have a distribution of  $v_1$ ,  $J_1$ ,  $M_1$  and  $v_2$ ,  $J_2$ ,  $M_2$ , respectively.

For derivation convenience, we consider a general objective function that is defined inside a region  $\Omega_2$  in Fig. 3 as

$$F = \int_{\Omega_2} f(\boldsymbol{B}(\boldsymbol{A}_2)) k d\Omega \quad , \tag{15}$$

where k is the localizing factor, which is used to select the integral domain for the objective function, where it is equal to 1. Except in this area, the localizing factor k is zero.

Firstly, the objective function is coupled with the magnetostatic governing equation using the Lagrange multiplier method as follows:

$$L(\mathbf{A}, \overline{\mathbf{A}}) = F + l(\overline{\mathbf{A}}) - a(\mathbf{A}, \overline{\mathbf{A}}) \quad . \tag{16}$$

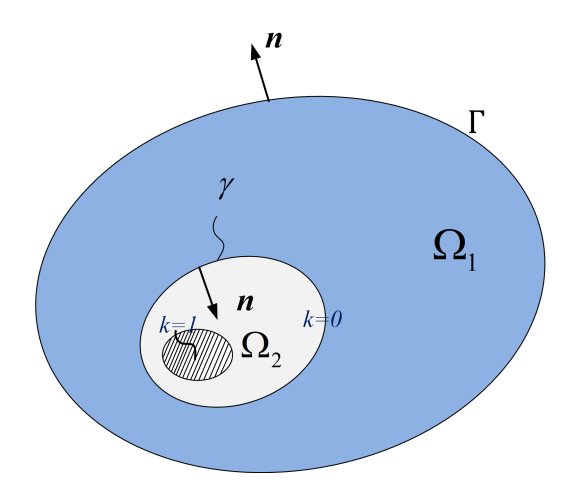


**FIGURE 3**: A schematic of the magnetostatic system interface.

Next, the material time derivative is utilized to derive the shape sensitivity [30, 33, 34]:

$$\frac{DL(A,\overline{A})}{Dt} = \frac{DF}{Dt} + \frac{Dl(\overline{A})}{Dt} - \frac{Da(A,\overline{A})}{Dt} \quad . \tag{17}$$

For conciseness, the derivative of the Lagrangian is directly presented as follows:

$$\frac{DL}{Dt} = \int_{\gamma} \frac{1}{\mu_0} \left( \frac{1}{\mu_r} - 1 \right) \boldsymbol{B}(\boldsymbol{A}_1) \cdot \boldsymbol{B}(\overline{\boldsymbol{A}}_2) V_n ds \quad , \tag{18}$$

where  $\gamma$  is the interface between the iron  $\Omega_1$  and the air  $\Omega_2$ . The adjoint variable  $\overline{A}_2$  can be obtained by solving the following equation with the corresponding boundary condition.

$$\int_{\Omega_{1}} \frac{1}{\mu_{1}} \boldsymbol{B}(\boldsymbol{A}_{1}) \cdot \boldsymbol{B}(\overline{\boldsymbol{A}}_{1}) d\Omega + \int_{\Omega_{2}} \frac{1}{\mu_{2}} \boldsymbol{B}(\boldsymbol{A}_{2}) \cdot \boldsymbol{B}(\overline{\boldsymbol{A}}_{2}) d\Omega 
= \int_{\Omega_{2}} \frac{\partial f}{\partial \mathbf{B}_{2}} \cdot \boldsymbol{B}(\dot{\boldsymbol{A}}_{2}) k d\Omega \quad ,$$
(19)

where  $\frac{\partial f}{\partial \mathbf{B}_2} = \left(\frac{\partial f}{\partial B_{2x}}, \frac{\partial f}{\partial B_{2y}}\right)^T$ . By plugging Equation (7) into Equation (18), the material derivative of Lagrangian can be assembled as

$$\frac{DL}{Dt} = \sum_{j=1}^{n} \dot{\mu}_{j}(t) \int_{\gamma} \left[ \frac{1}{\mu_{0}} \left( \frac{1}{\mu_{r}} - 1 \right) \boldsymbol{B}(\boldsymbol{A}_{1}) \cdot \boldsymbol{B}(\overline{\boldsymbol{A}}_{2}) \right] \frac{1}{|\nabla \Phi|} \Psi_{j}(\boldsymbol{x}) ds \quad .$$
(20)

Similarly, the material derivative of the volume constraint can be

formulated as

$$\frac{DV}{Dt} = \int_{\gamma} V_n ds = \int_{\gamma} \frac{1}{|\nabla \Phi|} \sum_{i=1}^{n} \dot{\mu}_j(t) \Psi_j(\mathbf{x}) ds \quad . \tag{21}$$

With the chain rule, the material derivatives of Lagrangian and volume constraint can also be expressed as

$$\frac{DL}{Dt} = \frac{\partial L}{\partial \mu(t)} \frac{\partial \mu(t)}{\partial t} = \frac{\partial L}{\partial \mu(t)} \dot{\mu}(t) \quad , \tag{22a}$$

$$\frac{DV}{Dt} = \frac{\partial V}{\partial \mu(t)} \frac{\partial \mu(t)}{\partial t} = \frac{\partial V}{\partial \mu(t)} \dot{\mu}(t) \quad . \tag{22b}$$

To solve the optimization problem (10), the advanced gradient-based optimizer, method of moving asymptotes (MMA) [35, 29], is implemented in this study. By comparing the corresponding parts of Eqs. (20), (21) and (22), the sensitivity of the objective function F and volume constraint V can be formulated as follows:

$$\frac{\partial F}{\partial \mu_j(t)} = \int_{\gamma} \left[ \frac{1}{\mu_0} \left( \frac{1}{\mu_r} - 1 \right) \boldsymbol{B}(\boldsymbol{A}_1) \cdot \boldsymbol{B}(\overline{\boldsymbol{A}}_2) \right] \frac{1}{|\nabla \Phi|} \Psi_j(\boldsymbol{x}) ds \quad , \tag{23a}$$

$$\frac{\partial V}{\partial \mu_i(t)} = \int_{\gamma} \frac{1}{|\nabla \Phi|} \Psi_j(\mathbf{x}) ds \quad . \tag{23b}$$

It is noted that the boundary integration in the above equation can be converted into a domain integration by using the Dirac delta function  $\delta$  as:

$$ds = \delta(\Phi) |\nabla \Phi| d\Omega. \tag{24}$$

In addition, the sensitivity of the distance regularization energy functional *R* can be derived as follows:

$$\frac{\partial R}{\partial \mu_i(t)} = -\nabla \cdot (d_p(|\nabla \Phi|)|\nabla \Phi|) \cdot \Psi_j(\mathbf{x}) \quad , \tag{25}$$

where  $d_p$  is defined as [28]

$$d_p(s) \triangleq \frac{p'(s)}{s},\tag{26}$$

where p'(s) is the first derivative of the regularization energy potential density defined in Eq.(14). Finally, the shape sensitivity

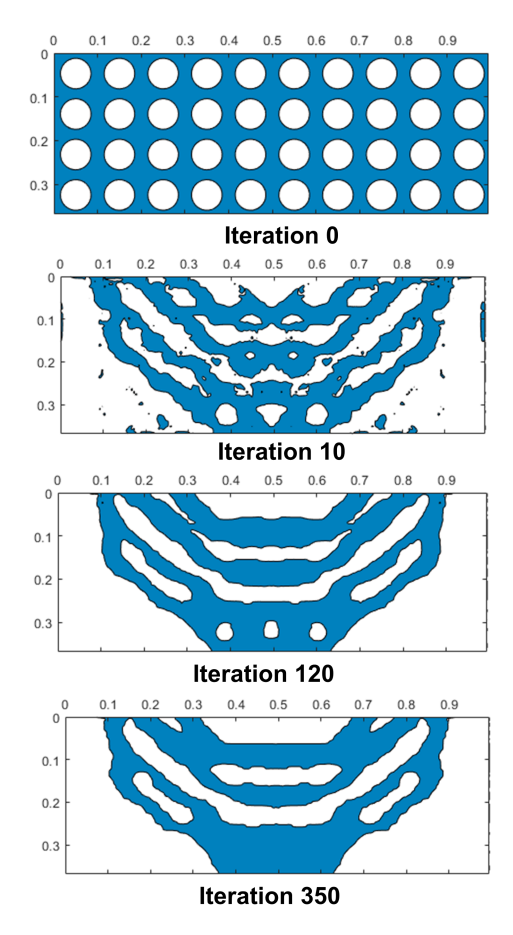


**FIGURE 4**: The optimization design evolution for SynRM design.

of the total objective function J coupling the distance regularization energy function R with the original objective function F can be expressed in the form of domain integration as:

$$\begin{split} \frac{\partial J}{\partial \mu_{j}(t)} &= \int_{\Omega} \left[ \frac{1}{\mu_{0}} \left( \frac{1}{\mu_{r}} - 1 \right) \boldsymbol{B}(\boldsymbol{A}_{1}) \cdot \boldsymbol{B}(\overline{\boldsymbol{A}}_{2}) \right] \delta(\boldsymbol{\Phi}) \Psi_{j}(\boldsymbol{x}) d\Omega \\ &+ w \frac{\partial R}{\partial \mu_{j}(t)} \quad , \end{split}$$
(27)

where w is the weighting factor. Similarly, the shape sensitivity of the volume constraint expressed in the form of domain integration is also given here:

$$\frac{\partial V}{\partial \mu_i(t)} = \int_{\Omega} \delta(\Phi) \Psi_j(\mathbf{x}) d\Omega \quad . \tag{28}$$

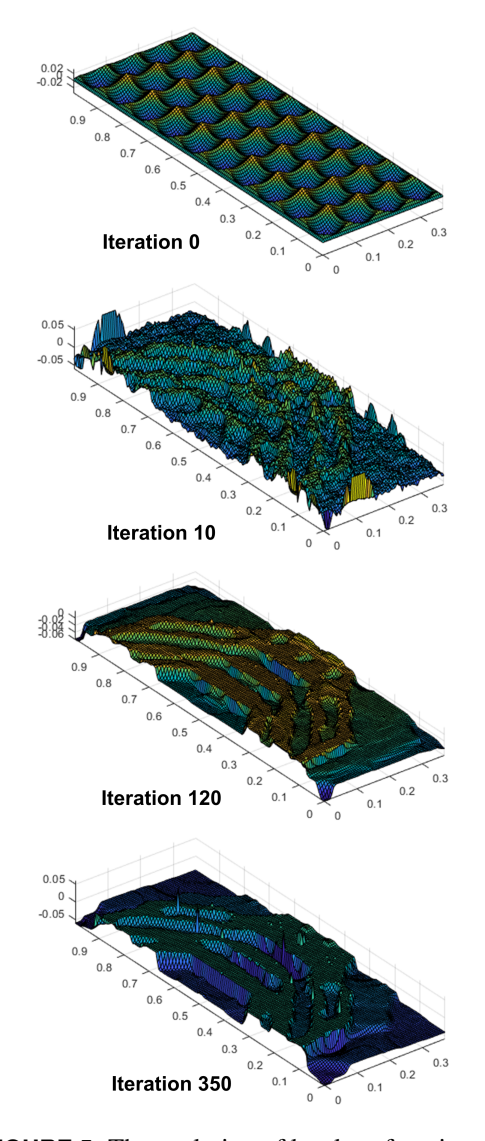


**FIGURE 5**: The evolution of level set function  $\Phi$ .

## 4 Design Example

The proposed design optimization method is applied to a four-pole Synchronous reluctance motor in Sec. 2. To obtain a symmetric design, only the left half domain is studied, and the design variable is symmetrically assigned along the axis of 45 degree, as shown in Fig. 1. The relative permeability of the material is interpolated using the Heaviside function of the level set function  $\Phi$ . The initial volume fraction of iron in the rotor is 0.6078, and the target volume fraction target is set to 0.4.

From Sec. 3.4, it is noted that the calculation of gradient and divergence is vital in the shape sensitivity analysis. In general, structured quadrilateral meshes have several advantages over triangle meshes when it comes to computing gradients and divergences. The gradient of a scalar function on a structured

quadrilateral mesh can be approximated using a bilinear interpolation scheme, which is simpler and more accurate than the linear interpolation scheme used for triangle meshes. In addition, the divergence of a vector field can be calculated using a simple finite difference scheme that takes advantage of the structured quadrilateral mesh. According to this, the conformal mapping theory [36, 37] is employed to parameterize the 2D triangle meshed irregular design domain onto a structured quadrilateral meshed rectangular domain, where the level set function is defined. Then, the proposed extended level set method is applied to the design in this study. For more details, readers are referred to [38, 39, 40, 41]. In the implementation process, the design domain is meshed with 11363 triangular elements before conformally mapped to a 0.3708  $m \times 1$  m rectangular domain, where the level set function is defined and discretized with  $65 \times 174$ grids.

In this study, a total of 7 rotor positions (every 10 degrees from 0 to  $60^{\circ}$ ) were investigated. Due to the rotational nature of the design domain, the meshes employed to discretize the said domain must undergo rotational movement. The rotation-moving mesh is expressed as

$$\begin{bmatrix} x_r \\ y_r \end{bmatrix} = \begin{bmatrix} \cos \theta - \sin \theta \\ \sin \theta & \cos \theta \end{bmatrix} \begin{bmatrix} x - X_p \\ y - Y_p \end{bmatrix} + \begin{bmatrix} X_p \\ Y_p \end{bmatrix}, \tag{29}$$

where  $x_r$  and  $y_r$  represent the mesh coordinates after rotation relative to a random point  $(X_p, P_p)$ . x and y are the mesh coordinates in the original design domain and  $\theta$  represents the mechanical rotation angle. Figure 4 shows the design evolution on the rectangular domain, and its corresponding level set function  $\Phi$  is given in Fig. 5. The design evolution in the rotor of SynRM after conformal mapping is illustrated in Fig. 6. The optimization history, including the average torque, torque variance, volume ratio, and distance regularization energy, is given in Fig. 7. The volume of the permanent magnet is 40.01% when the optimization ends. Since there is no least reluctance position in the initial design, the average reluctance torque is 0. After the optimization ends, the average torque increased to 14.71  $N \cdot m$ , and the torque variance converged at 1.21. In addition, the distance regularization energy R remains at a relatively low level, which guarantees the distance-regularized level set evolution during the optimization

To verify the effectiveness of the proposed method, we also investigated the torque performance of a reference synchronous reluctance motor with a multi-layer flux barrier, shown in Fig. 8. The same boundary conditions are applied to the reference model, and its calculated torque characteristics are compared with the optimized SynRM in Fig. 9. Our optimized model can generate an average torque at 14.88 N while the average torque of the reference model is 11.42 N, so it turns out that the average torque increased by 30.30%. The torque variance of the

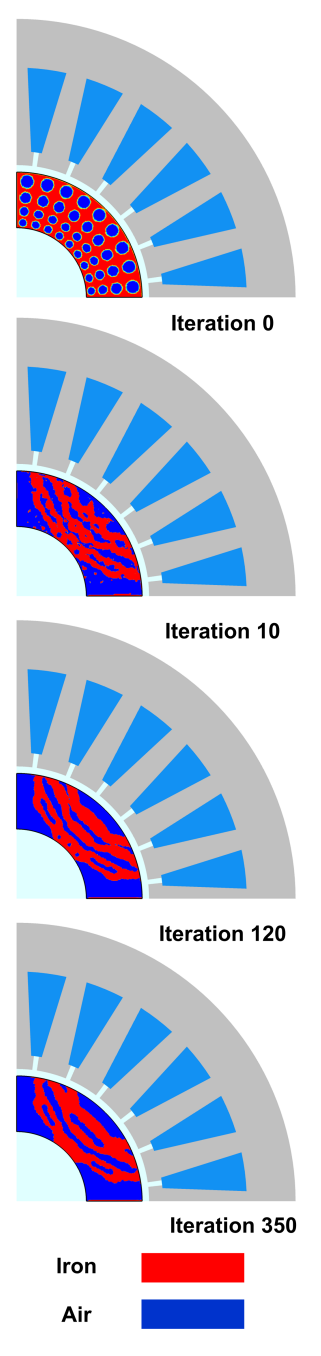


**FIGURE 6**: The design evolution in the rotor of SynRM.

optimized design is 0.228425, while the reference model only has 0.11 torque variance. One reason leading to this deficiency can attribute to the few rotor positions considered. In addition, an appropriate weight should be chosen to balance the average torque and torque variance in the objective function formulation.

Finally, the full 2.5D optimized rotor was extruded and assembled with the rotor bridge, shaft, and stator for unity, as

shown in Fig. 10.

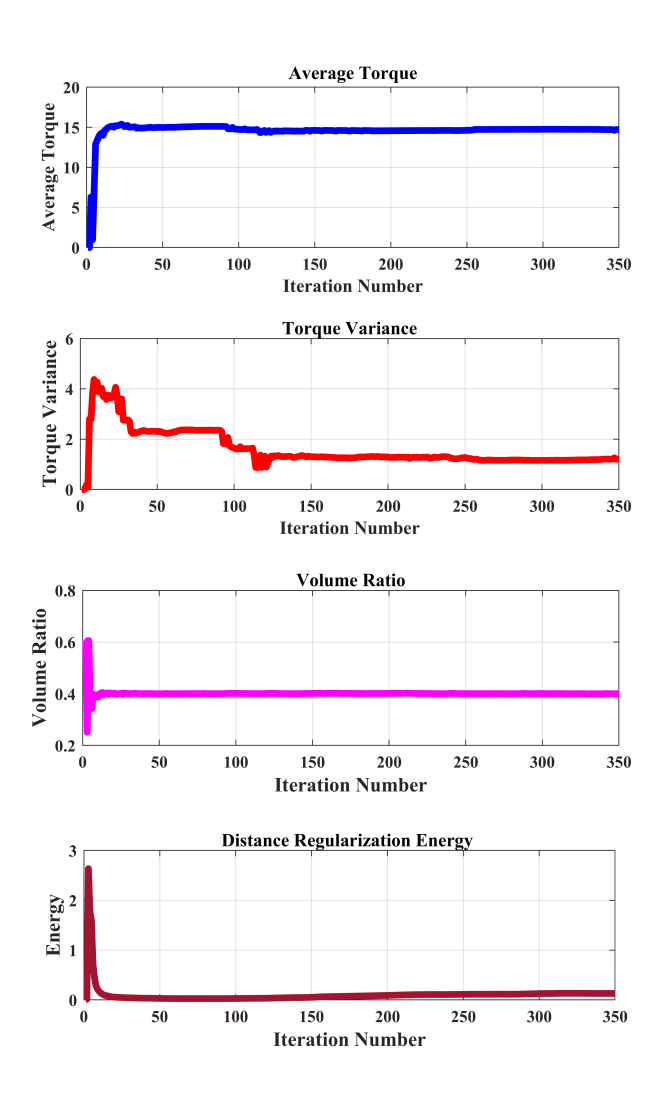


**FIGURE 7**: The iteration history for SynRM design.

#### 5 Conclusion and Future Work

The rotor structure of the four-pole synchronous reluctance motor (SynRM) was designed using the cardinal basis function (CBF) based level set method. Although the solver for the SynRM is a time-dependent study, a magnetostatic field analysis is carried out at every rotor position in this study. The design problem is reformulated to balance average torque improvement and ripple reduction. One numerical example was carried out to verify the proposed method. The torque performance of the optimized SynRM is compared with that of a reference model. Pre-

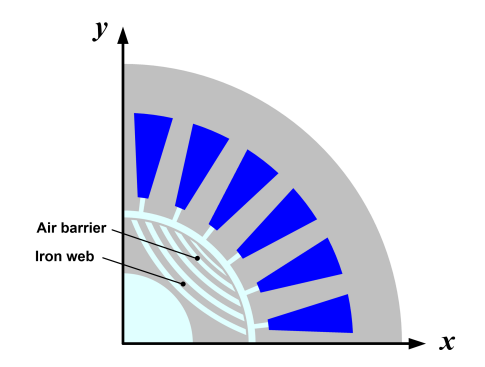


**FIGURE 8**: The CAD model of a reference SynRM.

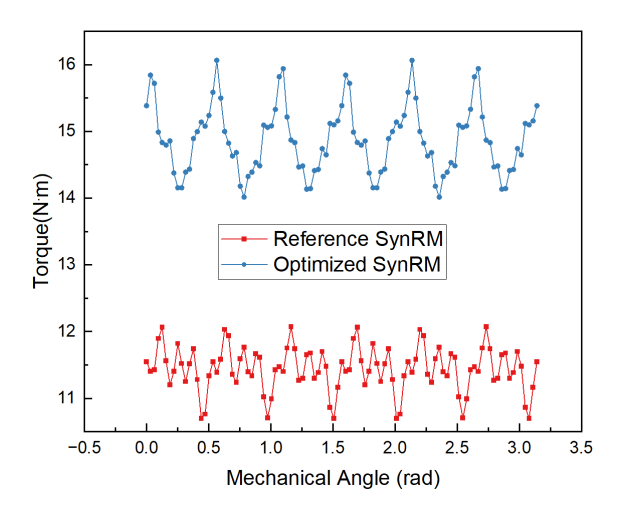


**FIGURE 9**: Torque performance comparison between reference and optimized SynRM.

liminary results show that the optimized SynRM has a 30.30% increase in average torque, along with a slight increase in torque ripple, compared to the reference model. Based on these, there is still much room for improvement in future studies. One of our efforts will incorporate the nonlinear B-H curve into the topology optimization of the rotor structure to accurately investigate the influence of magnetic saturation on torque performance. Besides, to further reduce the torque ripple, an increasing number of rotor positions should be considered in the objective function formulation, with attention to the issue of computational cost.

#### Acknowledgement

We would like to acknowledge the financial support provided by the National Science Foundation (CMMI-1762287; PFI-RP-2213852), GE Renewable Energy (Awards No.: 95031, 97223), the Advanced Energy Research and Technology Center (AERTC), and the Center for Integrated Electric Energy Systems

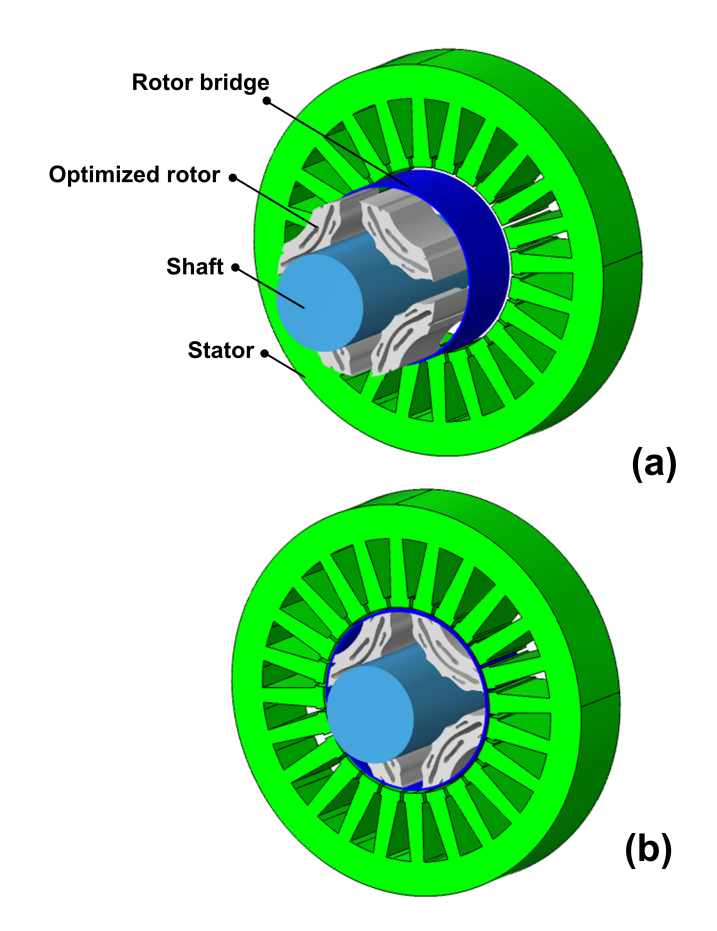


**FIGURE 10**: (a) The 3D components of optimized SynRM. (b) 3D assembly of optimized SynRM.

(CIEES) at the State University of New York (SUNY) at Stony Brook (SBU). We also extend our gratitude to Peter Donnelly, David Hamilton, Michael Antonucci, and Prathamesh Hajirnis at the SBU Office of Economic Development for their invaluable support throughout this project.

### **REFERENCES**

- [1] Pham, T., Kwon, P., and Foster, S. "Additive manufacturing and topology optimization of magnetic materials for electrical machines—a review". *Energies*, *14*(2), p. 283.
- [2] Betz, R. E., Lagerquist, R., Jovanovic, M., Miller, T. J., and Middleton, R. H. "Control of synchronous reluctance machines". *IEEE Transactions on Industry Applications*, **29**(6), pp. 1110–1122.
- [3] Bonthu, S. S. R., Arafat, A., and Choi, S. "Comparisons of rare-earth and rare-earth-free external rotor permanent magnet assisted synchronous reluctance motors". *IEEE Transactions on Industrial Electronics*, **64**(12), pp. 9729–9738.

- [4] Heidari, H., Rassõlkin, A., Kallaste, A., Vaimann, T., Andriushchenko, E., Belahcen, A., and Lukichev, D. V. "A review of synchronous reluctance motor-drive advancements". *Sustainability*, *13*(2), p. 729.
- [5] Bocker, J., and Mathapati, S. "State of the art of induction motor control". In 2007 IEEE International Electric Machines & Drives Conference, Vol. 2, IEEE, pp. 1459–1464.
- [6] Fei, W., and Luk, P. C.-K. "Torque ripple reduction of a direct-drive permanent-magnet synchronous machine by material-efficient axial pole pairing". *IEEE Transactions on Industrial Electronics*, **59**(6), pp. 2601–2611.
- [7] Park, J.-M., Kim, S. I., Hong, J. P., and Lee, J. H. "Rotor design on torque ripple reduction for a synchronous reluctance motor with concentrated winding using response surface methodology". *IEEE Transactions on Magnetics*, 42(10), pp. 3479–3481.
- [8] Lee, C., and Jang, I. G. "Multi-material topology optimization for the PMSMs under the consideration of the MTPA control". *Structural and Multidisciplinary Optimization*, **65**(9), p. 263.
- [9] Nishanth, F., Johnson, M., and Severson, E. L. "A review of thermal analysis and management of power dense electric machines". In 2021 IEEE International Electric Machines & Drives Conference (IEMDC), IEEE, pp. 1–8.
- [10] Lee, C., Lee, J., and Jang, I. G. "Topology optimization for the manufacturable and structurally safe synchronous reluctance motors with multiple iron webs and bridges". *IEEE Transactions on Industrial Electronics*, **70**(1), pp. 678–687
- [11] Lee, C., and Jang, I. G. "Topology optimization of multiple-barrier synchronous reluctance motors with initial random hollow circles". *Structural and Multidisciplinary Optimization*, *64*, pp. 2213–2224.
- [12] Okamoto, Y., Hoshino, R., Wakao, S., and Tsuburaya, T. "Improvement of torque characteristics for a synchronous reluctance motor using MMA-based topology optimization method". *IEEE transactions on magnetics*, *54*(3), pp. 1–4.
- [13] Yamashita, Y., and Okamoto, Y. "Design optimization of synchronous reluctance motor for reducing iron loss and improving torque characteristics using topology optimization based on the level-set method". *IEEE Transactions on Magnetics*, *56*(3), pp. 1–4.
- [14] Heo, S. H., Baek, M. K., Lee, K. H., Hong, S. G., and Park, I. H. "Shape and topology optimization of rotor in synchronous reluctance motor using continuum sensitivity and adaptive level set method". In 2013 International Conference on Electrical Machines and Systems (ICEMS), IEEE, pp. 129–133.
- [15] Kim, Y. S., and Park, I. H. "Topology optimization of rotor in synchronous reluctance motor using level set method and shape design sensitivity". *IEEE Transactions on Applied Superconductivity*, 20(3), pp. 1093–1096.

- [16] Sato, S., Sato, T., and Igarashi, H. "Topology optimization of synchronous reluctance motor using normalized Gaussian network". *IEEE transactions on magnetics*, *51*(3), pp. 1–4.
- [17] Takahashi, N., Yamada, T., and Miyagi, D. "Examination of optimal design of IPM motor using ON/OFF method". *IEEE Transactions on Magnetics*, **46**(8), pp. 3149–3152.
- [18] Okamoto, Y., Tominaga, Y., Wakao, S., and Sato, S. "Topology optimization of rotor core combined with identification of current phase angle in IPM motor using multistep genetic algorithm". *IEEE Transactions on Magnetics*, 50(2), pp. 725–728.
- [19] Choi, J. S., Izui, K., Nishiwaki, S., Kawamoto, A., and Nomura, T. "Topology optimization of the stator for minimizing cogging torque of IPM motors". *IEEE Transactions on Magnetics*, 47(10), pp. 3024–3027.
- [20] Tian, J., Zhuang, R., Cilia, J., Rangarajan, A., Luo, F., Longtin, J., and Chen, S. "Topology Optimization of Permanent Magnets for Generators Using Level Set Methods". In International Design Engineering Technical Conferences and Computers and Information in Engineering Conference, Vol. 86236, American Society of Mechanical Engineers, p. V03BT03A037.
- [21] Hermann, A. N. A., Mijatovic, N., and Henriksen, M. L. "Topology optimisation of PMSM rotor for pump application". In 2016 XXII International Conference on Electrical Machines (ICEM), IEEE, pp. 2119–2125.
- [22] Guo, F., Tang, N., and Brown, I. P. "Magneto-structural combined dimensional and topology optimization of interior permanent magnet synchronous machine rotors". *IEEE Transactions on Industry Applications*, 58(6), pp. 7241– 7250.
- [23] Mohamodhosen, B. S. B. "Topology optimisation of electromagnetic devices". PhD thesis, Ecole Centrale de Lille.
- [24] Lazarov, B. S., and Sigmund, O. "Filters in topology optimization based on Helmholtz-type differential equations". *International Journal for Numerical Methods in Engineering*, **86**(6), pp. 765–781.
- [25] Wang, M. Y., Wang, X., and Guo, D. "A level set method for structural topology optimization". *Computer methods in applied mechanics and engineering*, **192**(1-2), pp. 227–246.
- [26] Jiang, L., and Chen, S. "Parametric structural shape & topology optimization with a variational distance-regularized level set method". *Computer Methods in Applied Mechanics and Engineering*, **321**, pp. 316–336.
- [27] Jiang, L., Chen, S., and Jiao, X. "Parametric shape and topology optimization: A new level set approach based on cardinal basis functions". *International Journal for Numerical Methods in Engineering*, **114**(1), pp. 66–87.
- [28] Li, C., Xu, C., Gui, C., and Fox, M. D. "Distance regularized level set evolution and its application to image segmen-

- tation". *IEEE transactions on image processing*, **19**(12), pp. 3243–3254.
- [29] Svanberg, K. "MMA and GCMMA-two methods for non-linear optimization". *vol*, *1*, pp. 1–15.
- [30] Allaire, G., Jouve, F., and Toader, A.-M. "Structural optimization using sensitivity analysis and a level-set method". *Journal of computational physics*, **194**(1), pp. 363–393.
- [31] Safdari-Vaighani, A., Heryudono, A., and Larsson, E. "A radial basis function partition of unity collocation method for convection–diffusion equations arising in financial applications". *Journal of Scientific Computing*, **64**(2), pp. 341–367.
- [32] Adams, R. A., and Fournier, J. J., 2003. *Sobolev spaces*. Elsevier.
- [33] Choi, K. K., and Kim, N.-H., 2006. *Structural sensitivity analysis and optimization 1: linear systems*. Springer Science & Business Media.
- [34] Park, I. H., 2019. Design Sensitivity Analysis and Optimization of Electromagnetic Systems. Springer.
- [35] Svanberg, K. "The method of moving asymptotes—a new method for structural optimization". *International journal for numerical methods in engineering*, **24**(2), pp. 359–373.
- [36] Lui, L. M., Gu, X., Chan, T. F., Yau, S.-T., et al. "Variational method on riemann surfaces using conformal parameterization and its applications to image processing". *Methods and Applications of Analysis*, *15*(4), pp. 513–538.
- [37] Gu, X., Wang, Y., Chan, T. F., Thompson, P. M., and Yau, S.-T. "Genus zero surface conformal mapping and its application to brain surface mapping". *IEEE transactions on medical imaging*, 23(8), pp. 949–958.
- [38] Ye, Q., Guo, Y., Chen, S., Lei, N., and Gu, X. D. "Topology optimization of conformal structures on manifolds using extended level set methods (X-LSM) and conformal geometry theory". *Computer Methods in Applied Mechanics and Engineering*, *344*, pp. 164–185.
- [39] Tian, J., Zhao, X., Gu, X. D., and Chen, S. "Designing ferromagnetic soft robots (FerroSoRo) with level-set-based multiphysics topology optimization". In 2020 IEEE International Conference on Robotics and Automation (ICRA), IEEE, pp. 10067–10074.
- [40] Tian, J., Li, M., Han, Z., Chen, Y., Gu, X. D., Ge, Q., and Chen, S. "Conformal topology optimization of multi-material ferromagnetic soft active structures using an extended level set method". Computer Methods in Applied Mechanics and Engineering, 389, p. 114394.
- [41] Xu, X., Gu, X. D., and Chen, S. "Topology optimization of thermal cloaks in euclidean spaces and manifolds using an extended level set method". *International Journal of Heat and Mass Transfer,* 202, p. 123720.